Ultrasound in Medicine & Biology 000 (2023) 1–10

Contents lists available at ScienceDirect

Ultrasound in Medicine & Biology

journal homepage: www.elsevier.com/locate/ultrasmedbio

Original Contribution

The Effect of Spatial Velocity Gradients on Block-Matching Accuracy for Ultrasound Velocimetry

Jason Voorneveld *, Johan G. Bosch

Department of Biomedical Engineering, Thorax Center, Erasmus Medical Center, Rotterdam, The Netherlands

ARTICLE INFO

Keywords:
High-frame-rate ultrasound
Blood speckle tracking
Echo-particle image velocimetry
Ultrasound image velocimetry
Blood flow imaging
Vector flow Imaging
Spatial velocity gradient
Plane-wave compounding
Block matching

Objective: Block matching serves as the foundation for ultrasound velocimetry techniques such as blood speckle tracking and echo-particle image velocimetry. Any spatial velocity gradients (SVGs) inside a block-matching pair will result in tracking error, due to both the finite block size and the ultrasound point-spread-function. We assess, using an in silico sinusoidal flow phantom, the effect of SVG magnitude and beam-to-flow angle on block-matching bias and precision. Secondarily we assess the effect that SVGs have on velocimetry bias when using angled plane-wave compounding.
Methods: The magnitude and angle of SVGs were varied by adjusting the wavelength and direction of a sinusoidal flow profile. Scatterers displaced by this flow profile were used for simulating ultrasound radio frequency data at discrete time points. After beamforming, the 2-D flow field was estimated using block matching. Two imaging sequences were tested, a single plane-wave and a three-angled plane-wave.
Results: Smaller sinusoidal flow wavelengths resulted in increased bias and reduced precision, revealing an inverse relationship between sinusoidal flow wavelength and tracking error, with median errors ranging from 69%–90% for the smallest flow wavelengths (highest SVGs) down to 3%–5% for the largest (lowest SVGs). The SVG angle was also important, in which lateral SVGs (with axially oriented flows) resulted in significant speckle decorrelation and high tracking errors in regions with high SVGs. Conversely, axial SVGs (laterally oriented flow) experienced higher bias in the peak velocity regions of the flow profile. Coherent compounding resulted in higher velocity errors than using a single transmission for lateral SVGs but not for axial SVGs.
Conclusion: The highest SVGs that could be measured with ≤10% error was when the sinusoidal flow wavelength was less than 20 times the ultrasound pulse wavelength. The clinical significance is that the high SVGs present in high kinetic energy flows, such as severe carotid stenosis and aortic regurgitation, will limit the ability to accurately quantify the velocities in these flow structures.

Introduction

Block-wise tracking methods, such as (blood) speckle tracking and echo-particle image velocimetry (echoPIV), are emerging alternatives to ultrasound Doppler for blood flow measurement. Block-matching methods have the advantage of being able to measure both the magnitude and angle of the velocity vector while also being robust to aliasing [1]. The basic principle of both echoPIV (and speckle tracking) is to subdivide the acquired images into discrete blocks and find the most likely location of each block's texture in the subsequent frame, thereby measuring the speckle displacement [2]. For small inter-frame scatterer displacements, the speckle motion follows the underlying scatterer motion, allowing for the estimation of the blood velocity in each block.

However, in the presence of a spatial velocity gradient (SVG), there is not a single displacement that is valid for all velocity streamlines in the block, resulting in bias and increased variance in the displacement estimate. In the field of optical particle image velocimetry (PIV), Scarano [3] found that larger block sizes resulted in increased underestimation of peak displacements in flows with SVGs. In ultrasound imaging the spatial resolution of the imaging system, approximated by the point-spread-function (PSF), will also act as a filter on the spatial velocity frequencies present in the region of interest. Friemel et al. [4] have shown that the magnitude and direction of SVGs influence the correlation of the speckle pattern over time, where purely axial motion with a lateral gradient resulted in more rapid speckle decorrelation than lateral motion with an axial gradient (Fig. 1). Foster et al. [5] found that the presence of SVGs in a Doppler range-cell reduced measurement precision. Similarly, Wu et al. [6] found that a laterally oriented flow with a parabolic profile could be accurately estimated, but large errors were associated with the same profile oriented axially (in the linear gradient regions).

When imaging blood flows in the heart and large blood vessels, the high blood velocity necessitates the use of high-frame-rate ultrasound imaging, where plane-wave or diverging-wave transmit sequences are used, instead of the conventional focussed-wave imaging technique. The use of unfocussed transmit waves has the drawback of reduced image quality and thus multiple waves from different virtual sources are often

* Corresponding author. Biomedical Engineering, Thorax Center, Erasmus Medical Center, EE-2302, Wytemaweg 80, Rotterdam 3015 CN, Netherlands.
E-mail address: j.voorneveld@erasmusmc.nl (J. Voorneveld).

https://doi.org/10.1016/j.ultrasmedbio.2023.09.002
Received 2 July 2023; Revised 17 August 2023; Accepted 2 September 2023

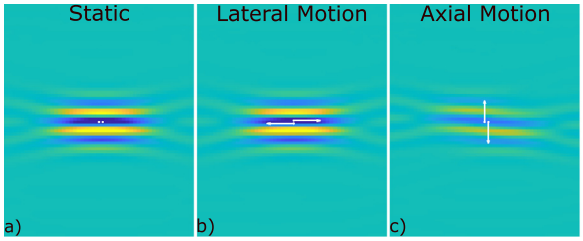

Figure 1. Coherently compounded (three angles) beamformed radio frequency data of two scatterers with different motion patterns: (a) no motion, (b) one third λ/PRI relative motion in lateral direction and (c) one third λ/PRI relative motion in axial direction. All images share the same dynamic range. Inspired by Friemel et al. [4]. PRI, pulse repetition interval.

combined, for instance via angular-compounding or synthetic aperture imaging [7,8]. However, these methods assume that scatterers are static between a set of transmissions used to form a higher-resolution PSF. Previous studies have identified that imaging artefacts and low-pass velocity filtering occur when this stationarity assumption is violated [9–11], but these studies focussed on uniform flows and did not investigate the additional effect of spatial velocity gradients on the process of coherent summation.

In the work described here, we investigated the effect of SVGs on block-matching accuracy and precision using an in silico flow phantom inspired by Scarano [3]. We also investigate the effect that angular compounding and the method of compounding has on block-matching accuracy in the presence of SVGs. The primary objective of this study was to determine how SVGs affect the accuracy and precision of block matching and secondarily to determine how angular compounding is affected by the magnitude and direction of SVGs.

Methods

The in silico framework for simulating fluid motion, ultrasound radio frequency (RF) data acquisition, image formation, speckle tracking and error analysis is described in this section. Briefly, a flow field propagates scatterers that are used for simulating ultrasound back-scattered RF data on a frame-by-frame basis. The RF data are then beamformed before speckle tracking and the estimated velocity fields are compared with the originally defined flow field.

Sinusoidal flow phantom

The main principle of the sinusoidal flow phantom (Fig. 2) is that the degree of SVGs present in the flow field varies by the wavelength of the sinusoid (Λ), which is related to the ultrasound pulse wavelength (λ) using a scalar multiplicand (c):

$$\Lambda = c\lambda \tag{1}$$

Smaller values of c result in higher SVG magnitudes and vice versa.

The steady-state flow field was simulated in 3-D with 3 principal axes ($\hat{\mathbf{i}}, \hat{\mathbf{j}}, \hat{\mathbf{k}}$). The stream-wise ($\hat{\mathbf{j}}$) velocity component of the flow field was modulated along the gradient axis ($\hat{\mathbf{i}}$) in a sinusoidal pattern. No gradient was present along the other principal axes and all other velocity components were 0. The velocity ($\hat{\mathbf{v}}$) at point [i, j, k] was computed using

$$\hat{\mathbf{v}}\begin{cases} v_i = 0 \\ v_j = a\cos(2\pi i/\Lambda) \\ v_k = 0 \end{cases} \tag{2}$$

where a is peak velocity amplitude (λ/pulse repetition interval [PRI]). This results in a velocity gradient ($\nabla\hat{\mathbf{v}}$) [s^{-1}] at point [i, j, k]:

$$\nabla\hat{\mathbf{v}}\begin{cases} \dfrac{\partial v}{\partial i} = \dfrac{-2\pi a\sin(2\pi i/\Lambda)}{\Lambda} \\ \dfrac{\partial v}{\partial j} = 0 \\ \dfrac{\partial v}{\partial k} = 0 \end{cases} \tag{3}$$

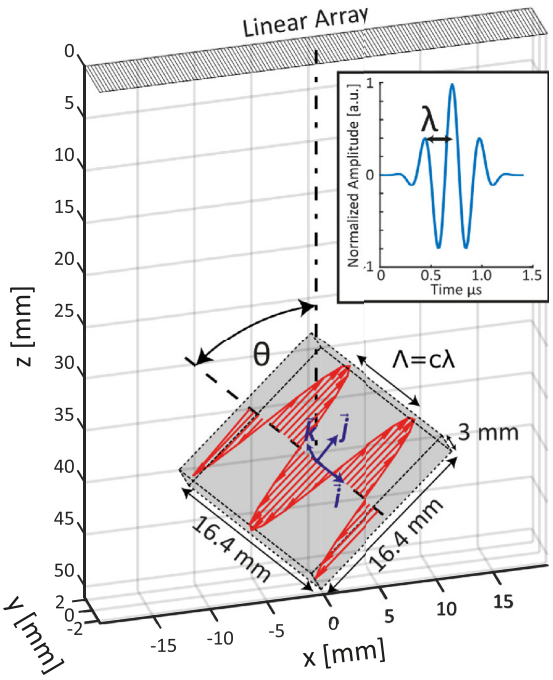

Figure 2. The simulated flow field with a sinusoidal velocity profile along the $\hat{\mathbf{i}}$ axis. The flow field is rotated relative to the simulated linear array with beam-to-flow angle θ. The wavelength of the sinusoidal pattern (Λ) is made to be relative to the transmitted pulse wavelength (λ). Inset: Simulated 5 MHz transmit pulse.

The phantom was then transformed into the transducer's reference frame (Cartesian):

$$\hat{\mathbf{v}}_{\mathbf{x,y,z}} = \begin{bmatrix} \cos\theta & 0 & \sin\theta \\ 0 & 1 & 0 \\ -\sin\theta & 0 & \cos\theta \end{bmatrix} \hat{\mathbf{v}}_{\mathbf{i,j,k}} + [x_0, y_0, z_0] \tag{4}$$

where θ is the rotation angle around the $\hat{\mathbf{j}}$ axis (adjusting the beam-to-flow angle) and [x_0, y_0, z_0] is a translation (between the origins of the probe and phantom). In this study a fixed translation of [0, 0, 40 mm] was used.

Ultrasound simulations

Scatterers were uniformly distributed into a cuboidal region ($16.4 \times 3 \times 16.4$ mm^3) at a density of 10 scatterers per resolution cell to simulate fully developed speckle. Scatterers were propagated in the flow field over 30 transmit-receive events, where the RF back-scatter from the scatterers was simulated using Field II [12,13]. The sampling frequency, medium sound speed and frequency-independent attenuation were set to 100 MHz, 1540 m/s and 0.5 dB/cm, respectively.

Fully developed speckle was confirmed by computing the mean-to-standard deviation ratio of the envelope of beamformed RF signal to be 1.91 ± 0.15 (assessed over 100 randomly distributed blocks of ≈ 3 × 3 mm^2), which was sufficiently close to the theoretically expected value of 1.91 [14].

Probe

A 128-element linear array transducer (pitch = λ = 308 µm) was simulated with a kerf of 30 µm. The element height was 5 mm, which provided a natural elevation focus at approximately 20 mm depth. The −6 dB elevational beam width was 2.5 ± 0.6 mm over the phantom region of interest (≈ 30–50 mm).

Ultrasound sequence

Two plane-wave sequences were tested: one using a single transmit steered at 0°, and a three-angled transmit scheme [−6.7°, 0°, 6.7°]. This angle sequence was used as a trade-off between PSF, frame rate and keeping the region of interest (*green box* in Fig. 3) insonified for all angles.

For both sequences, a Tukey apodization window ($\alpha = 0.5$) was used in transmit, over the full aperture. A three-cycle Hanning tapered pulse with 50% bandwidth was used (see inset of Fig. 2).

Beamforming

Beamforming was performed (in the XZ plane, Y = 0) using the standard delay-and-sum implementation of the UltraSound ToolBox [15]. A Tukey apodization window (cosine fraction = 0.5) was used in receive, with an f-number of 1.1 (computed using the directivity of the elements, as recommended by Perrot et al. [16]). A square pixel size of $\lambda/6$ (≈ 51 μm) was used for beamforming, as recommended by Saris et al. [17].

Compounding methods

Two compounding methods were tested: (i) coherent compounding [7] and (ii) correlation compounding [18,19]. For coherent compounding the beamformed RF data were summed for all angles before speckle tracking, so block matching was performed between compounded plane-wave images. For correlation compounding, instead of coherently summing separate angles in the spatial domain, the correlation maps of each angle are averaged after performing cross-correlation between like-angle pairs. The difference between these two compounding methods is that coherent compounding assumes that there is negligible scatterer displacement between angled acquisitions, while correlation compounding only assumes that there is negligible acceleration.

Speckle tracking

Speckle tracking was performed using a 2-D echoPIV implementation. Because no ultrasound contrast agent was used, this is equivalent to a 2-D blood speckle tracking implementation. Two sets of images (reference and target) were subdivided into equally sized square blocks with a 75% overlap. The cross-correlation of corresponding blocks was then calculated (block matching), where the peak of the cross-correlation function corresponded to the displacement of the speckle between those two blocks [2].

An iterative block-matching approach was used, meaning that the block matching was repeated multiple times, using the previous iteration's displacement estimation as input for deforming the target image set (using cubic interpolation). Six iterations were performed, with the square block size (l × l) halving in size every second iteration (*i.e.*, $l = 8 \rightarrow 8 \rightarrow 4 \rightarrow 4 \rightarrow 2 \rightarrow 2\lambda$).

This scheme was found optimal on average for all flow directions and flow wavelengths (Λ); see Appendix S1 (online only) for more details.

As the flow was steady over time, all frames were used for correlation averaging, where the correlation maps of multiple frame-pairs are averaged together before determining the displacement ($30/N_{angles}$ frames in total).

Sub-pixel interpolation was performed using a 2 × 3 parabolic fitting (independent three-point fitting in both x and z). The final output was a 75 × 75 rectilinear grid of vectors with a spacing of 205 × 205 μm.

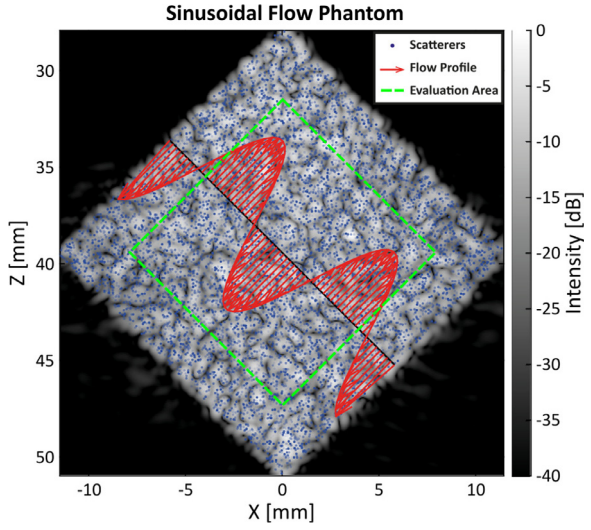

Figure 3. B-mode image of 45° rotated phantom with scatterers (*blue dots*) and flow pattern (*red arrows*) overlaid. *Green box* indicates the area used for accuracy assessment. Note that scatterers are shown in the XZ plane but are uniformly distributed along the y-axis.

Experimental design

In this study, we performed three different experiments (constant and experimental parameters are summarized in Tables 1 and 2, respectively):

1. Assessing the effect of SVG magnitude and direction on tracking error for a single-angle plane-wave sequence. Λ/λ = [2.5, 5,10, 20, 40] with gradient angles (d) of 0°, 45° and 90°.
2. Assessing if the tracking error would be equivalent in the lateral and axial directions if the flow wavelength was varied as a ratio of the PSF dimension in each direction (Λ/l_{PSF}) instead of the pulse wavelength (as in Experiment 1). For axial SVGs ($\theta = 0°$), the gradients align with the axial PSF ($l_{psf} = 1$; Fig. 4c); thus, Λ/λ remained the same as in item 1, whereas, for lateral SVGs ($\theta = 90°$), the gradients align with the lateral PSF ($l_{PSF} = 1.9$; Fig. 4b); thus, $\Lambda/\lambda \approx$ [5, 10, 20, 40, 80]. This ensured that the SVG magnitudes were constant relative to the anisotropic ultrasound PSF.
3. Assessing the effect of angled plane-wave compounding. Simulations using Λ/λ = [2.5, 5, 10, 20, 40] and θ = [0°, 90°] were simulated for a three-angled plane-wave sequence and compared with the single angle sequence of item 1. Both coherent and correlation compounding were tested.

Table 1
Constant properties

Medium	Values
Sound speed (m/s)	1540
Density (kg/m^3)	1020
Attenuation (dB/m)	50
Probe	
Number of elements	128
Pitch = λ (μm)	308
Element width (μm)	[278, 5000] (x, y)
Sequence	
Angular decimation factor	10
Transmit apodization window	Tukey ($\alpha = 0.5$)
Receive apodization window	Tukey ($\alpha = 0.5$)
Receive f-number	1.1
Pulse repetition frequency (Hz)	10,000
Speckle tracking	
Similarity measure	Normalized cross-correlation
Overlap (%)	75
Image deformation	Cubic interpolation
Square block size (λ)	$8 \rightarrow 8 \rightarrow 4 \rightarrow 4 \rightarrow 2 \rightarrow 2$
Phantom	
Maximum velocity (λ/PRI)	1/3

PRI, pulse repetition interval.

Table 2
Experimental variables

Variable	Values
Experiment 1: Effect of spatial velocity gradient magnitude and direction	
Λ/λ	2.5, 5, 10, 20, 40
θ (°)	0, 45, 90
Number of angles	1 [0°]
Experiment 2: Effect of anisotropic PSF	
Λ/l_{PSF}	2.5, 5, 10, 20, 40
θ (°)	0, 90
Number of angles	1 [0°]
Experiment 3: Effect of compounding	
Λ/λ	2.5, 5, 10, 20, 40
θ (°)	0, 90
Number of angles	1 [0°], 3 [−6.7°, 0°, 6.7°]
Compounding method	Coherent, correlation

PSF, point-spread-function.

In all cases, the peak velocity amplitude of the sinusoidal flow pattern was fixed (a = 1/3A/PRI ~ 1.0 m/s). A more extensive experiment on the effect of peak displacement amplitude is available in Appendix S2 (online only).

Error analysis

Only the inner two-thirds of the phantom extent (≈ 11 × 11 mm^2) were used for error analysis to avoid spurious vectors near the edge of the phantom. Error was assessed using the range-normalized magnitude of the error between the speckle tracking and ground truth velocityvectors:

$$\textbf{Error} = \frac{\|\mathbf{V_{st}} - \mathbf{V_{gt}}\|}{max(\|\mathbf{V_{gt}}\|)} \times 100\% \quad (5)$$

where V_{st} and V_{gt} refer to the co-located speckle tracking and ground truth fields of N vectors, each with [x, y] components. Error is a vector of N scalars representing the error at each point in the flow grid. The errors were normalized to the maximum of the ground truth velocities and presented as a percentage.

Bias was assessed using the median error and precision using the interquartile range: (median [25th percentile, 75th percentile]).

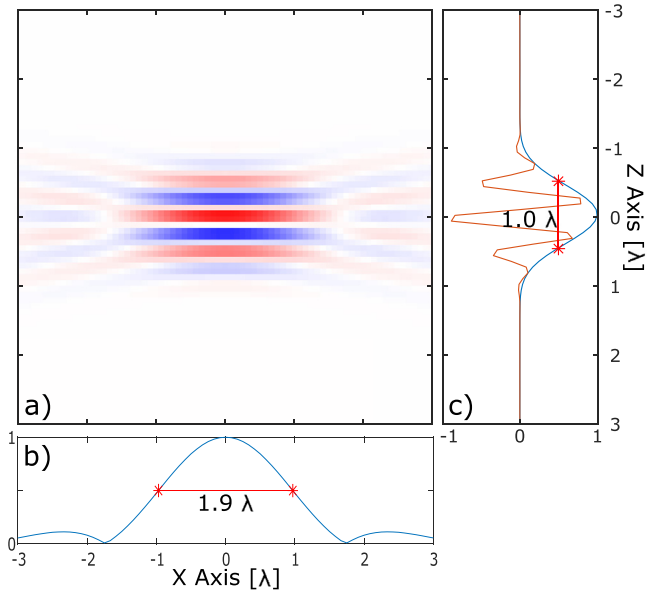

Figure 4. (a) Beamformed radio frequency data of a single scatterer at 40 mm depth using a single plane-wave sequence. (b, c) Full-width half-maximum of the PSF (referred to as l_{PSF}) along the x- and z-axes, respectively. The PSF for the three-angled sequence was similar, with an l_{PSF} of 1.7, 1.0 λ [x, z]. PSF, point-spread-function.

Results

Effect of SVG magnitude and direction

Using the data of Experiment 1, the effect of SVG magnitude and angle can be observed in Figure 5 and Table 3 (using a single transmit angle). Laterally oriented flows (*green lines* in Fig. 5) tend to underestimate the peak velocities of the flow profile more than axially oriented flows (with diagonal flows falling in between). However, axially oriented flows (*blue lines* in Fig. 5) have increased variance compared to diagonal and lateral flows and overestimate velocities near the zero-crossings of the flow profile (Fig. 5c). The correlation profile (maximum-normalized cross-correlation values) for axial flows was strongly modulated by the velocity profile (Fig. 5g–k). However, for lateral flows, this was not the case, as correlation profile values remained high (≥0.9) even when error was high (Fig. 5c, 5h).

In Experiment 2, the anisotropic PSF dimensions (Fig. 4) were taken into account, and the flow wavelength was varied as a function of the PSF width in the gradient direction instead of the pulse wavelength. We can observe in Figure 6a that the axially oriented flows (lateral SVGs) experienced lower error on average than laterally oriented flows (axial SVGs), which is in contrast to the results obtained in Experiment 1 (Fig. 5a). Additionally, we see that the errors in the peaks of the velocity profile are lower for axially than laterally oriented flows (Fig. 6b). However, in the zero-crossing regions of the velocity profile (region where SVGs are locally the highest), axially oriented flows experience higher errors than laterally oriented flows.

Effect of SVGs on angular compounding

In Experiment 3, the effect that SVGs have when using angular compounding for speckle tracking is shown in Figure 7. For axial flows, using a single plane-wave resulted in the lowest errors, followed by correlation compounding and then coherent compounding (Fig. 7a). Observing the velocity magnitude profiles for axial flow (Fig. 7c–g), it can be seen that correlation compounding had lower error at the peaks of the velocity profile than coherent compounding, whereas coherent compounding experienced lower error near the zero-crossings of the profile than correlation compounding. Using a single transmit angle resulted in the lowest error. The three-angled sequences experienced stronger modulation of their correlation profile than the single-angled sequence (Fig. 7m–q).

For lateral flows, there was a smaller effect of angular compounding on tracking accuracy (Fig. 7h–l), where correlation and coherent compounding only provided minor improvements to peak velocity accuracy over the single transmit sequence in medium/high SVG cases (Fig. 7i, 7j). There was also no appreciable modulation of the correlation profile (Fig. 7r–v), except in the case of very strong SVGs ($\Lambda/\lambda \leq 5$).

Speckle correlation

Figure 8 shows the cross-correlation maps (used to estimate the displacement vector) for the first iteration of the block-matching sequence, where the difference between axial and lateral flows in the peak gradient (zero-crossing of the velocity profile) and peak velocity (zero-crossing of the velocity gradient profile) can be appreciated. The speckle motion for these different flow regions, flow directions and number of transmit angles is shown in Video S1 (online only). Note the splitting of the correlation peak in the axially oriented peak gradient region when using correlation compounding. Using coherent compounding, in the same region, results in vertical correlation ridges due to the vertical dark bands in the image (caused by motion-induced speckle decorrelation; see Video S1c, S1d). Laterally oriented flows are not as affected by compounding, but blurring of the correlation peak is observed for the three-angle sequences. In all cases, the single angle produces the most prominent cross-correlation peak.

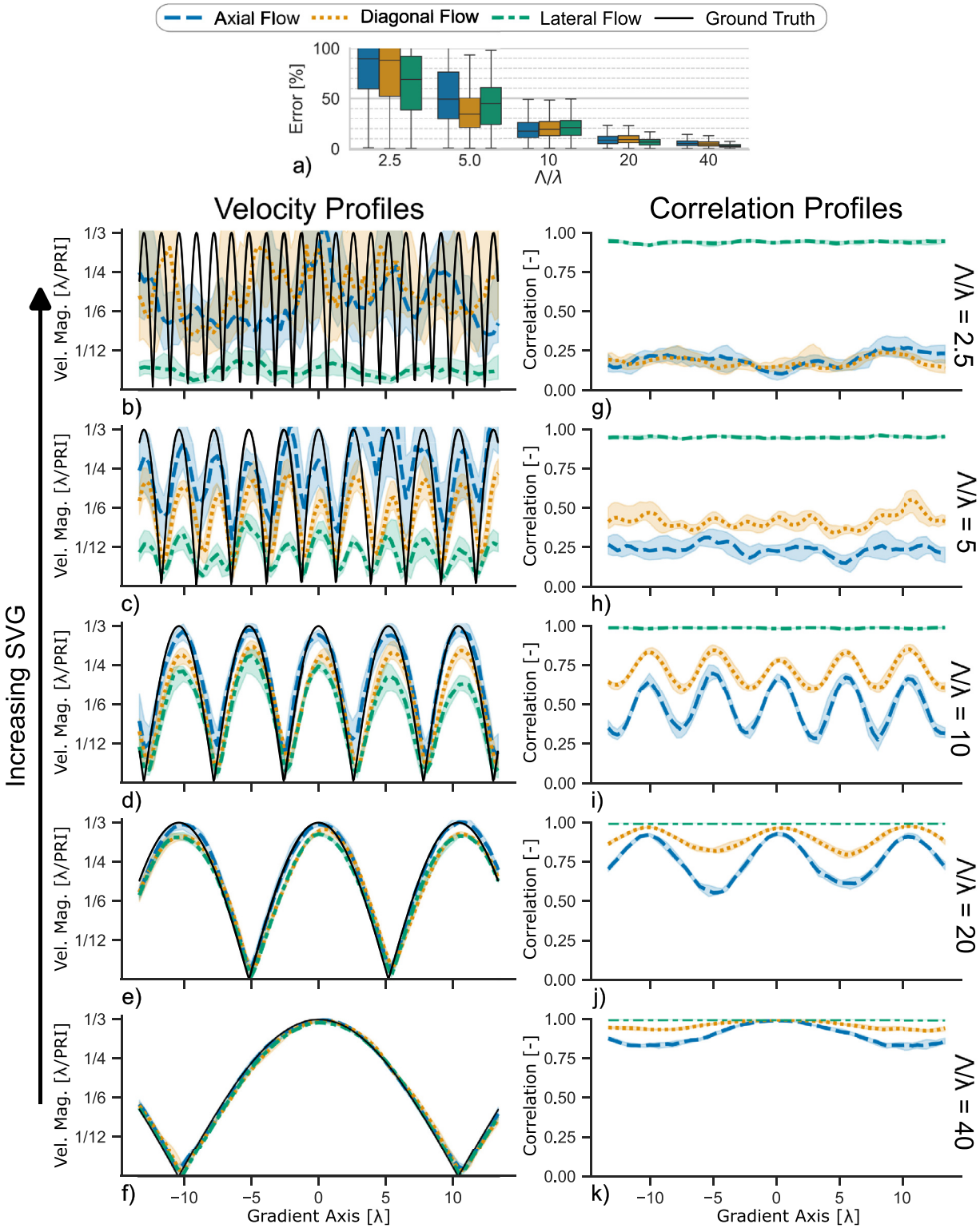

Figure 5. (a) Error per flow wavelength ratio. (b–f) Velocity magnitude and (g–k) maximum cross-correlation profiles along the gradient axis. *Lines* represent median and *shaded areas* extend to the interquartile range. Hue indicates the direction of flow (gradient is perpendicular to this direction).

Discussion

We have shown that the magnitude and angle of SVGs can severely impact block-matching accuracy and precision. We also observed that using angled plane-wave compounding in the presence of SVGs results in reduced accuracy and precision for lateral SVGs, compared with a single angle.

Beam to velocity-gradient angle

Block-matching methods are often referred to as angle-independent velocity estimators; however, it is clear from these results that tracking accuracy is affected by the orientation of spatial velocity gradients. For axially oriented gradients, with the fluid flowing laterally, the majority of error occurs in the peak-velocity region of the flow profile (Figs. 5c–f

Table 3
Experiment 1 results

Λ/λ	Median error [interquartile range] (%)		
	Axial flow	Diagonal flow	Lateral flow
2.5	89.5 [59.5, 130.2]	88.2 [52.2, 136.4]	69.0 [38.6, 92.0]
5	49.2 [29.8, 76.2]	34.4 [21.1, 50.2]	45.0 [24.2, 60.9]
10	17.3 [10.7, 26.1]	19.2 [12.6, 26.9]	20.7 [13.2, 27.8]
20	8.2 [4.9, 12.3]	9.0 [5.8, 12.7]	6.5 [3.6, 8.9]
40	4.8 [2.8, 7.3]	4.5 [2.6, 6.7]	2.6 [1.5, 3.7]

and 6b). While for laterally oriented gradients, with axially flowing fluid, errors are highest around the zero-crossings of the flow profile (where the maximum gradients occur; see Figs. 5c–e and 6c). In the case of laterally oriented gradients with axial flow, the scatterers' relative positions within the resolution cell change over time, which then interact with the phase sensitive RF pulse, causing significant speckle pattern changes from frame to frame (Video S1b). This results in the observed error increase in high SVG regions. For axially oriented gradients with lateral flow, the relative positions of the scatterers also change over time, but their phase with respect to the incident RF pulse is constant, avoiding speckle decorrelation (Video S1f).

Anisotropic PSF

One may expect that if the SVG magnitudes were equal relative to the PSF in each direction then the error would also be equivalent in each direction. From Experiment 2, where the gradients were scaled relative to the PSF dimension (l_{psf}), we see that the anisotropic PSF alone does not explain the angle dependence, although overall accuracy is now higher for axial flows (lateral SVGs) than for lateral flows (axial SVGs) (see differences between Figs. 5a and 6a). Accuracy in the peak-velocity regions is higher for axially oriented flows (Fig. 6b), while the accuracy in the peak-gradient (zero-crossings of the velocity profile) regions is still lower (Fig. 6c) than for laterally oriented flows.

The difference in peak-velocity accuracy between axial and lateral flows (where gradients are ≈ 0) is likely due to the anisotropic PSF as well, where a larger PSF dimension results in a bias towards lower velocities. This bias likely occurs during the sub-pixel estimation step of the

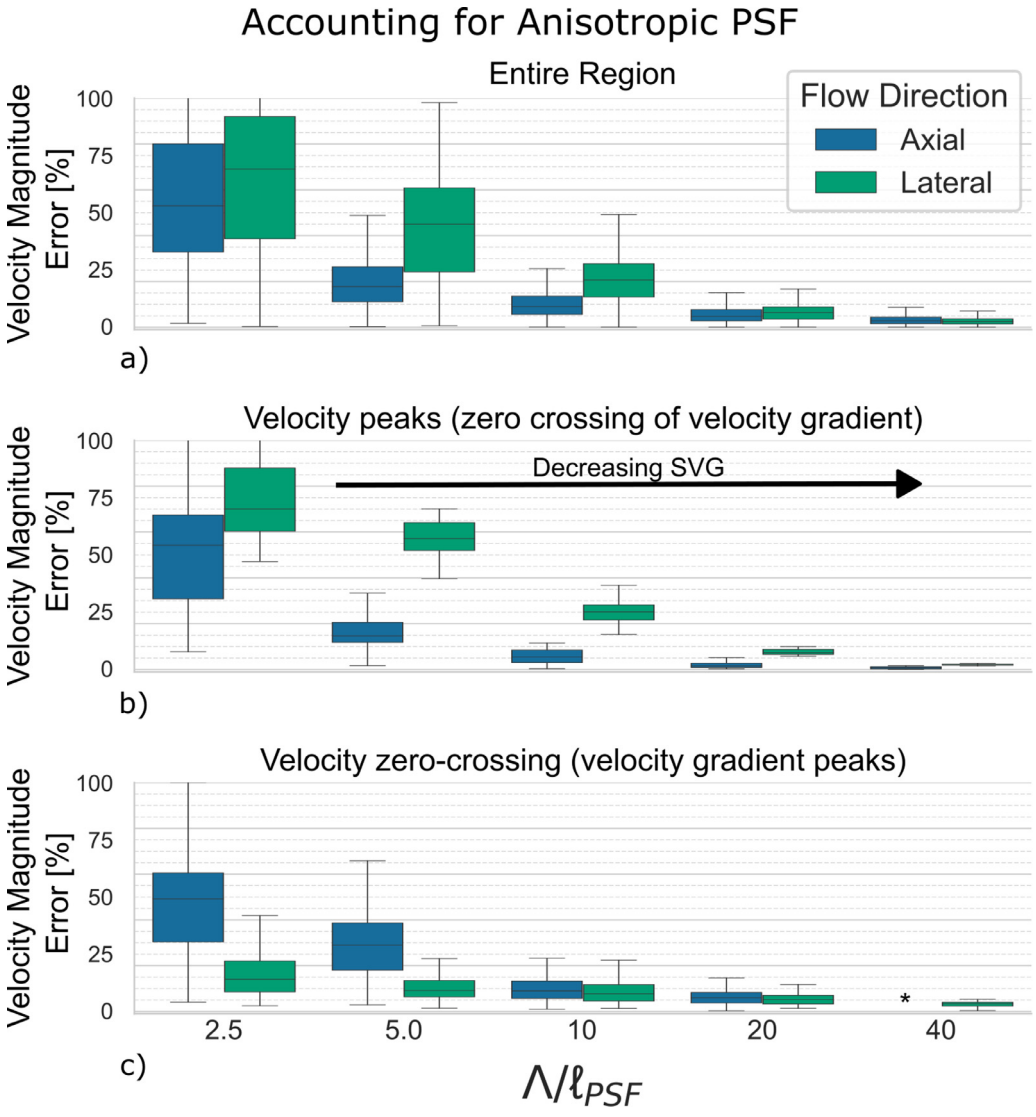

Figure 6. Analysis of velocimetry error when directional anisotropy of the PSF is accounted for (flow wavelength varied as a function of l_{PSF} in each direction independently). Axially oriented flows have lower errors on average (a) and in the regions of the velocity peaks (b) than laterally oriented flows. However, the error in the high SVG regions (c) is higher for axial flows, even after taking the anisotropic PSF into account. *Flow wavelength too large for zero-crossing data to fit in the field of view. PSF, point-spread-function; SVG, spatial velocity gradient.

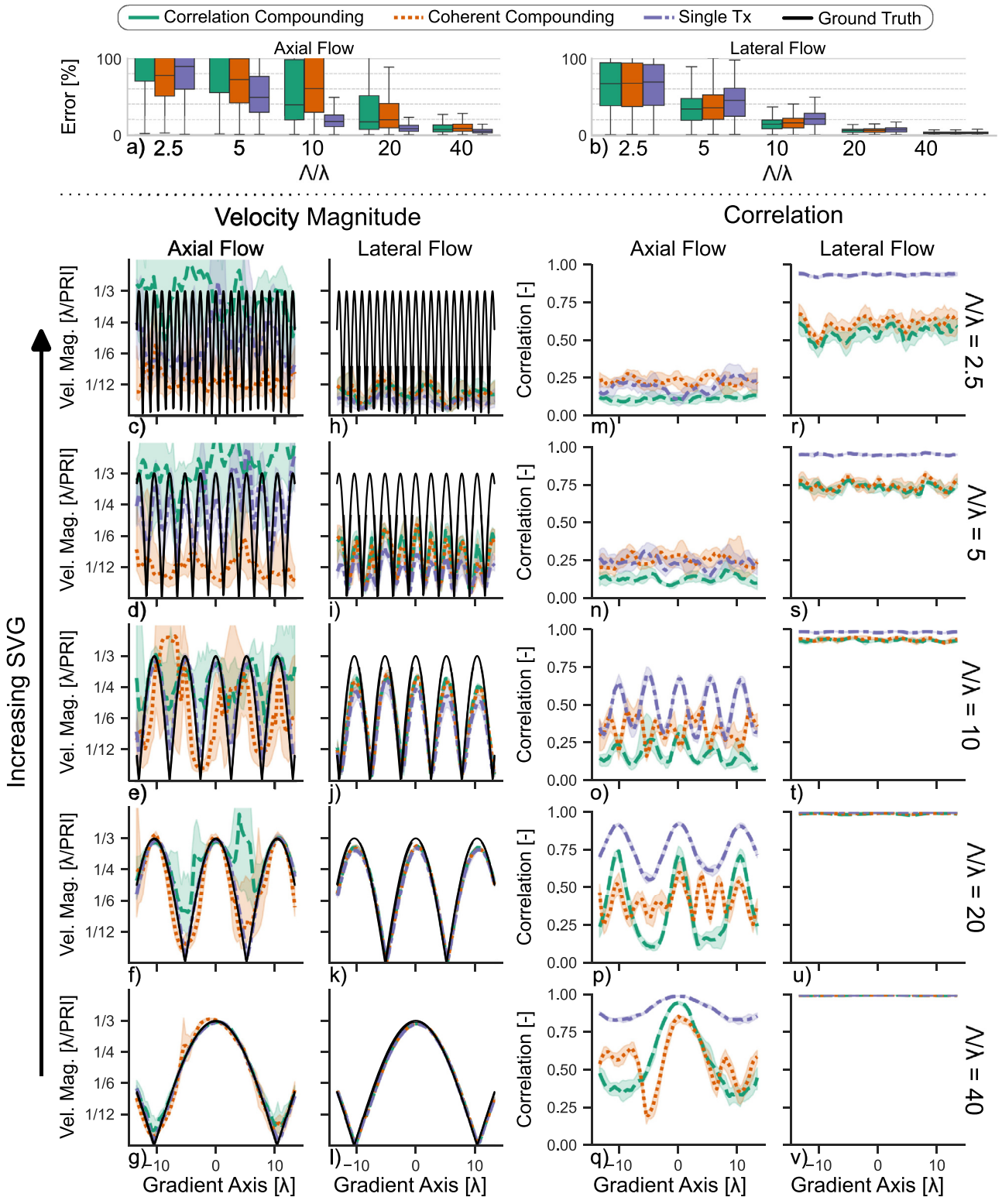

Figure 7. Effect of spatial velocity gradients and angular compounding technique on speckle tracking error for maximum displacement = 1/3 λ/PRI. Boxplots showing median and interquartile range of error for axially (a) and laterally oriented (b) flows. (c–l) Median velocity magnitude profiles for axial (c–g) and lateral (h–l) flows with *shaded region* indicating the interquartile range. (m–v) Maximum normalized cross-correlation profiles for axial (m–q) and lateral (r–v) flows. PRI, pulse repetition interval.

velocimetry process, where it is known from optical PIV that larger PSFs (called particle image diameter in the PIV field) result in higher errors [20].

In the peak-gradient regions (Fig. 6c), only lateral SVGs result in speckle decorrelation, due to the interaction between the varying relative axial scatterer locations and the phase sensitive RF pulse. These results corroborate existing literature on the angle-dependent decorrelation effect of SVGs when imaging with ultrasound [4–6]. Similarly, Rossi et al. [21] found that blood speckle tracking accuracy was severely reduced when imaging a parabolic flow profile (elevational SVGs) across

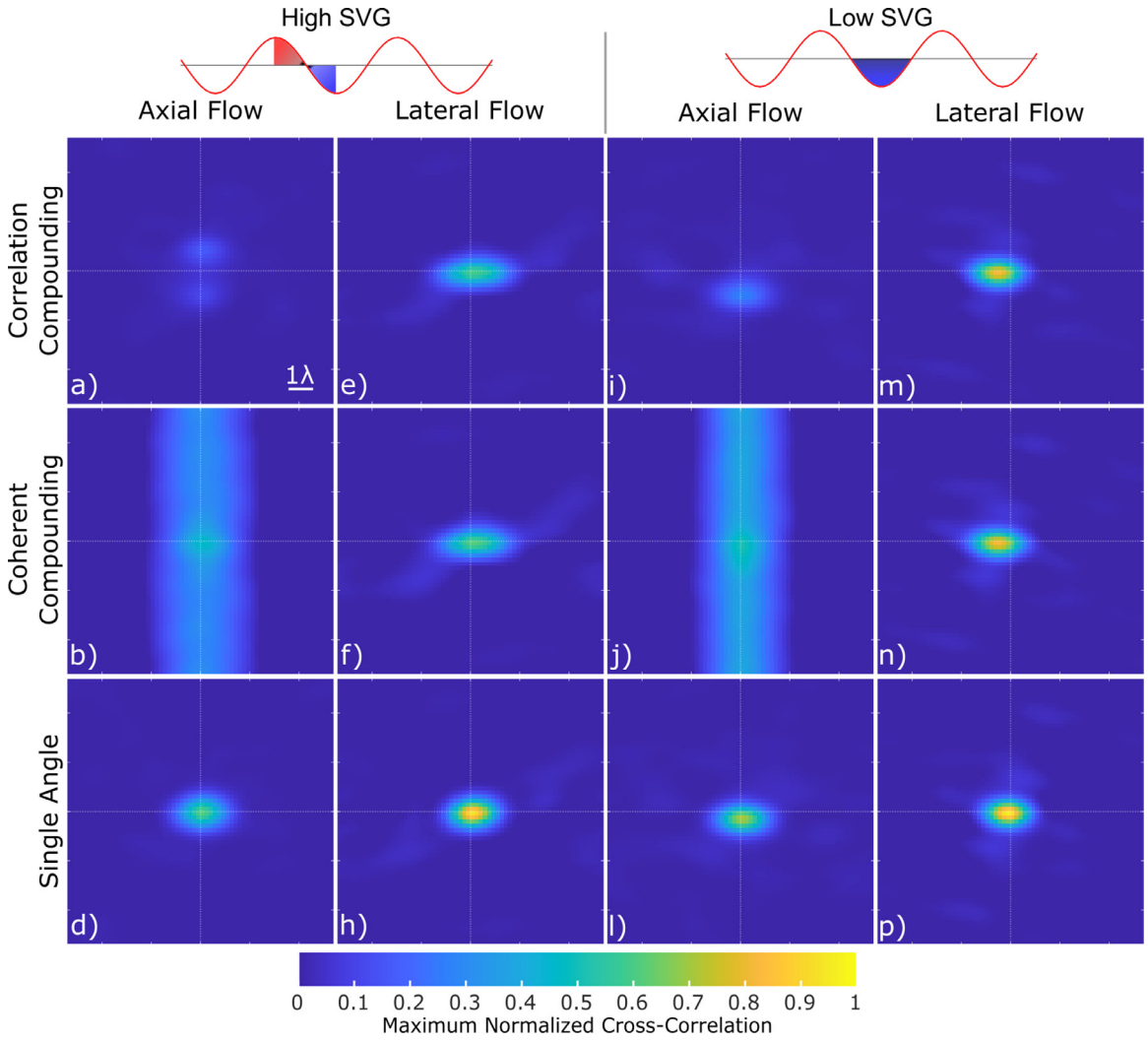

Figure 8. Mean normalized cross-correlation maps centred around the peak gradient region (a–h) and peak velocity region (i–p) for axial flow (laterally oriented gradients: a–d and i–l) and lateral flow (axially oriented gradients: e–h and m–p). *Shaded regions* in sinusoidal profiles at the top of the figure indicate the extents of the interrogation window and the stream-wise velocity for the peak gradient and peak velocity regions. Displacement amplitude = 1/3 λ/PRI and Λ/λ = 20. PRI, pulse repetition interval.

the elevational beam width, compared with a flat flow profile (no elevational SVGs).

While our simulations have been performed without SVGs along the elevational axis, we expect that a similar relationship will hold between elevational gradients with axial flows and lateral gradients with axial flows (decorrelation due to out-of-phase summation of scatterers within a resolution cell).

Thus, for measurement of axially oriented flows, one should be mindful of the relationship between the PSF and corresponding SVGs in the cross-beam direction. Reducing the width of the lateral PSF, by decreasing the f-number, increasing the transmit frequency or enlarging the receive aperture (either physically or by optimizing receive apodization), may help to reduce tracking errors associated with SVGs.

Gradient magnitude

By decreasing Λ/λ, the SVG magnitude is increased independently of the velocity magnitude. For an accuracy of ≈90%, the minimum Λ/λ achievable was 20, which increased to 40 for a more stringent requirement of ≈95% accuracy. In general, the trend was that error halved when Λ/λ was doubled.

Effect of angular compounding method

For lateral SVGs (axial flow), it is clear from Figure 7 (and Appendix S2) that the three-angled sequences (whether using correlation or coherent compounding) resulted in increased error and variance compared to a single-angled sequence. Note the reduced maximum cross-correlation values around the zero-crossings of the velocity profile for correlation compounding, compared with coherent compounding (Fig. 7m–q). Looking at the correlation map in the zero-crossing region for correlation (Fig. 8a) and coherent (Fig. 8b) compounding, the reason for the increased variance and error can be appreciated: the correlation map of the correlation compounding sequence splits in two (*i.e.*, into a positive and negative displacement peak), as opposed to the correlation map for coherent compounding, which forms a vertical "ridge" (due to the motion-induced out-of-phase RF summation) but still maintains a single peak centred around zero displacement. Put more simply, by increasing the number of angles, the time between frames is increased, which allows for larger relative scatterer motion within the PSF, resulting in more speckle decorrelation between frames.

For axial SVGs (lateral flow), the choice of compounding method was far less impactful, with both methods performing equivalently. This can be attributed to the relatively wide lateral beam-width modulation,

which coherently sums even for high velocities. (In Appendix S2, in which higher velocities are tested, the beginning of incoherence can be observed in Fig. S2v for the three-angled sequences.) Here the improved image resolution (reduced PSF width) afforded by the angular compounding results in slightly improved tracking accuracy (Fig. 7b).

Note that there have been solutions proposed to reduce coherent compounding artefacts associated with scatterer motion, including modified transmission orders of the different angles [9,22], motion compensation [9–11,22] and use of interleaved transmit sequences [8]. How these methods perform in the presence of strong flow gradients is currently unknown, although any motion compensation requirements may be hindered by the speckle decorrelation that occurs in the case of high lateral SVGs.

In practically all cases, a single plane-wave acquisition scheme provided the lowest bias and highest precision.

Correlation profiles

The maximum normalized cross-correlation values obtained during block matching are often used as an indicator of tracking quality. Here we observed that the correlation values obtained using block matching did not correlate at all with the tracking accuracy of laterally oriented flows. For instance, see Figure 5g–h (*green line*), in which correlation values of ≥0.9 were consistently achieved even though errors were high (Fig. 5b, 5c; *green line*). Thus, the correlation values obtained should be used with caution when used as a surrogate for tracking accuracy.

Clinical implications

There are a few important clinical implications that are revealed by this study. First, the dependence on SVG direction for tracking accuracy implies that the imaging view should be carefully selected depending on the flow aspect of interest. For instance, in wall shear rate or wall shear stress measurements, velocity profiles are required near the vessel wall (where the SVGs are maximized), implying that the vessel should be aligned so that the blood flows laterally relative to the transducer (SVGs aligned axially). Note that there will still be the issue of wall-filter and multiple reflection artefacts to contend with, but the effect of SVGs on speckle decorrelation will be minimized in this orientation. Another example is in cardiac imaging, where apical views are most often used for vector flow imaging to capture the flow in and out of the left ventricle. In this case, the flow will be aligned axially (SVGs aligned laterally), leading to spurious vector measurements at the edges of the jet flow profiles, where SVGs are expected to be high.

We also observed that using angular compounding resulted in significantly higher error and variance for axial flows with lateral SVGs. This implies that when imaging high SVG flow structures, such as left ventricular filling and ejection, very few or no compounding angles should be used. Another solution is to rearrange the imaging view so that these flow structures are oriented laterally rather than axially (*e.g.*, by using a parasternal long axis view instead of apical views).

For the linear array simulated in this study, we observed that the flow wavelength (Λ) should be at least 20 times the pulse wavelength (λ) for ≤10% error. For vascular flow, where a parabolic flow profile is often used as a simplification, only one side of the sinusoidal profile is required, meaning that the flow profile width can be $\leq 10\lambda$. To extend this concept further, it is more appropriate to evaluate estimation error as a function of Λ/l_{PSF} because the lateral PSF is not solely determined by the pulse wavelength, especially in cardiac imaging using phased arrays. Going further with the assumption of parabolic flow profiles, we can determine what Λ/l_{PSF} values and their associated errors can be expected for typical high velocity flow structures (Fig. 9). The Λ/l_{PSF} and error values in Figure 9 are optimistic as parabolic flow profiles are not often encountered in high-velocity cardiovascular flows [4]; thus, the SVGs are expected to be higher in practice. Additionally, Figure 9 does not take into account the influence of SNR, clutter, clutter-filtering

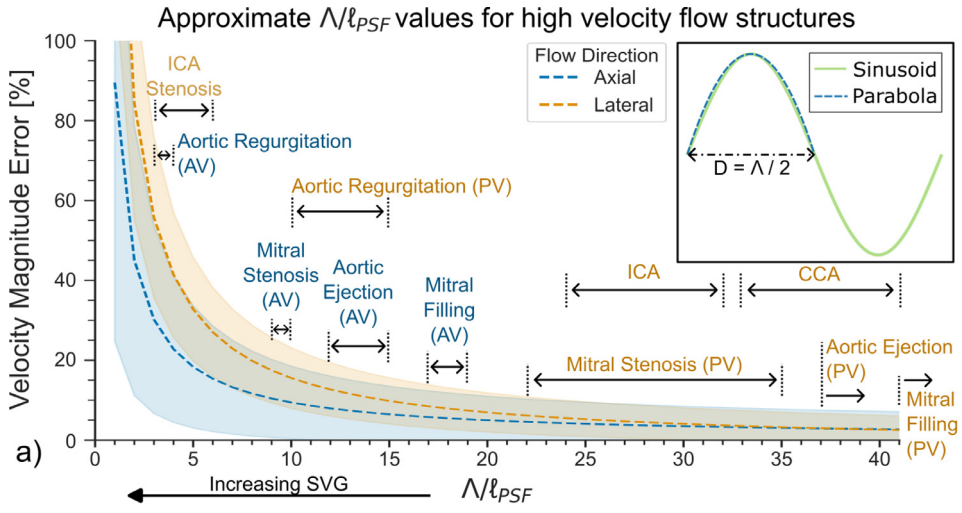

Carotid

Location	λ [μm]	ℓ_{PSFx} [λ]	ℓ_{PSFz} [λ]	D [mm]
CCA	308	-	1.0 ↔ 1.3	6.3
ICA	308	-	1.0 ↔ 1.3	4.9
ICA Stenosis	308	-	1.0 ↔ 1.3	1.0

Cardiac

Location	λ [μm]	ℓ_{PSFx} [λ]	ℓ_{PSFz} [λ]	D [mm]
Aortic Ejection	616	4.9 ↔ 5.9	1.3 ↔ 2.0	22.6
Aortic Regurgitation	616	4.9 ↔ 5.9	1.3 ↔ 2.0	6.2
Mitral Filling	616	4.4 ↔ 4.9	1.3 ↔ 2.0	25.2
Mitral Stenosis	616	4.4 ↔ 4.9	1.3 ↔ 2.0	13.8

b)

Figure 9. (a) Indicative Λ/l_{PSF} values for common high velocity flow structures of interest (assuming parabolic flow profiles with diameter D; see inset). *Dashed curve* indicates the inverse proportional fit to the data, with *shaded regions* indicating the uncertainty of the fit. (b) Values used to produce Λ/l_{PSF} estimates in (a). For cardiac cases, both apical view (AV) and parasternal view (PV) options are shown, where the gradient axis is aligned with the PSF along the x-axis for AV and z-axis for PV. Carotid and cardiac references obtained from two studies [23,24] and five studies [25–29], respectively. CCA, common carotid artery; ICA, internal carotid artery; PSF, point-spread-function.

or beamforming errors, which will increase velocimetry errors by different extents depending on the imaging situation. However, Figure 9 does show that SVGs can be expected to be a limiting factor for accurately assessing pathological flow structures (such as regurgitant and stenotic jets). For cardiac imaging, it is also interesting to note that even though the expected median errors are lower for axially oriented flows, it may be more beneficial to image flow in a parasternal view, so that the flow gradients through the valves can align with the axial PSF, rather than the much wider lateral PSF when imaging apically.

Note that the sinusoidal flow phantom was chosen so that the SVG strength could be varied independently of displacement amplitude and also relative to the ultrasound pulse wavelength. However, the flow patterns produced by this phantom are not physiological. They are intended to only serve as a tool for determining whether the SVGs present in a given physiological flow scenario will be a limiting factor for a given imaging system.

Conclusions

We have shown that both the magnitude and beam-to-flow angle of the SVGs in a flow structure influence block-matching accuracy and precision. Axially oriented flows, with lateral SVGs, were most affected by SVG magnitude, where out-of-phase summation of backscattered RF resulted in significant speckle decorrelation. On the contrary, laterally oriented flows, with axial SVGs, were not affected by speckle decorrelation but tended to have better velocity estimates in the high gradient regions but underestimated peak velocities more than for axial flows. We have also shown that angular compounding can degrade tracking performance for axial flows with lateral SVGs. We demonstrated that the minimum wavelength of the sinusoidal flow profile that can be measured with $\leq$10% error was 20 times the pulse wavelength (for a 128-element λ-pitch linear array).

Conflict of interest

The authors declare no competing interests.

Acknowledgments

The work described in this article was funded by project X-Flow of the research program Ultra-X-Treme (P17-32), which is financed by the Dutch Research Council (NWO). It was also funded by the Dutch Heart Foundation (Hartstichting) as part of project number 03-004-2022-0044.

Data availability statement

Data can be made available on reasonable request to the corresponding author of this study.

Supplementary materials

Supplementary material associated with this article can be found in the online version at doi:10.1016/j.ultrasmedbio.2023.09.002.

References

[1] Swillens A, Segers P, Torp H, Løvstakken L. Two-dimensional blood velocity estimation with ultrasound: speckle tracking versus crossed-beam vector doppler based on flow simulations in a carotid bifurcation model. IEEE Trans Ultrason Ferroelectr Freq Control 2010;57:327–39. doi: 10.1109/TUFFC.2010.1413.
[2] Introduction to speckle tracking in cardiac ultrasound imaging Garcia D, Lantelme P, Soloux E., Loizou CP, Pattichis CS, D'hooge J Handbook of speckle filtering and tracking in cardiovascular ultrasound imaging and video. Hertfordshire, UK: Institution of Engineering and Technology; 2018. p. 571–598.
[3] Scarano F. Theory of non-isotropic spatial resolution in PIV. Experiments in Fluids 2003;35:268–77.
[4] Friemel BH, Bohs LN, Nightingale KR, Trahey GE. Speckle decorrelation due to two-dimensional flow gradients. IEEE Trans Ultrason Ferroelectr Freq Control 1998;45:317–27. doi: 10.1109/58.660142.
[5] Foster SG, Embree PM, O'Brien WD. Flow velocity profile via time-domain correlation: error analysis and computer simulation. IEEE Trans Ultrason Ferroelectr Freq Control 1990;37:164–75. doi: 10.1109/58.55306.
[6] Wu SY, Wang SL, Li PC. Performance evaluation on high frame-rate speckle tracking. Proceedings IEEE Ultrasonics Symposium 2009:2375–8.
[7] Montaldo G, Tanter M, Bercoff J, Benech N, Fink M. Coherent plane-wave compounding for very high frame rate ultrasonography and transient elastography. IEEE Trans Ultrason Ferroelectr Freq Control 2009;56:489–506. doi: 10.1109/TUFFC.2009.1067.
[8] Jensen JA. Estimation of high velocities in synthetic-aperture imaging I: theory. IEEE Trans Ultrason Ferroelectr Freq Control 2019;66:1024–31. doi: 10.1109/TUFFC.2019.2906384.
[9] Denarie B, Tangen TA, Ekroll IK, Rolim N, Torp H, Bjåstad T, et al. Coherent plane wave compounding for very high frame rate ultrasonography of rapidly moving targets. IEEE Trans Med Imaging 2013;32:1265–76. doi: 10.1109/TMI.2013.2255310.
[10] Stanziola A, Toulemonde M, Li Y, Papadopoulou V, Corbett R, Duncan N, et al. Motion artifacts and correction in multipulse high-frame rate contrast-enhanced ultrasound. IEEE Trans Ultrason Ferroelectr Freq Control 2019;66:417–20. doi: 10.1109/TUFFC.2018.2887164.
[11] Ekroll IK, Voormolen MM, Standal OK, Rau JM, Lovstakken L. Coherent compounding in doppler imaging. IEEE Trans Ultrason Ferroelectr Freq Control 2015;62:1634–43. doi: 10.1109/TUFFC.2015.007010.
[12] Jensen JA. FIELD: a program for simulating ultrasound systems. Med Biol Eng Comput 1996;34(Suppl. 1):351–2.
[13] Jensen JA, Svendsen NB. Calculation of pressure fields from arbitrarily shaped, apodized, and excited ultrasound transducers. IEEE Trans Ultrason Ferroelectr Freq Control 1992;39:262–7. doi: 10.1109/58.139123.
[14] Wagner R, Smith S, Sandrik J, Lopez H. Statistics of speckle in ultrasound B-scans. IEEE Transactions on Sonics and Ultrasonics 1983;30:156–63. doi: 10.1109/T-SU.1983.31404.
[15] Rodriguez-Molares A, Rindal OMH, Bernard O, Liebgott H, Austeng A, Lovstakken L. The ultrasound toolbox. In: Paper presented at: July 9, 2017 IEEE International Ultrasonics Symposium (IUS); 2017.
[16] Perrot V, Polichetti M, Varray F, Garcia D. So you think you can DAS? a viewpoint on delay-and-sum beamforming. Ultrasonics 2021;111:106309. doi: 10.1016/j.ultras.2020.106309.
[17] Saris AECM, Fekkes S, Nillesen MM, Hansen HHG, De Korte CL. A PSF-shape-based beamforming strategy for robust 2D motion estimation in ultrafast data. Applied Sciences 2018;8:429. doi: 10.3390/app8030429.
[18] Leow CH, Tang MX. Spatio-temporal flow and wall shear stress mapping based on incoherent ensemble-correlation of ultrafast contrast enhanced ultrasound images. Ultrasound Med Biol 2018;44:134–52. doi: 10.1016/j.ultrasmedbio.2017.08.930.
[19] Voorneveld J, Muralidharan A, Hope T, Vos HJ, Kruizinga P, van der Steen AFW, et al. High frame rate ultrasound particle image velocimetry for estimating high velocity flow patterns in the left ventricle. IEEE Trans Ultrason Ferroelectr Freq Control 2018;65:2222–32. doi: 10.1109/TUFFC.2017.2786340.
[20] Westerweel J. Theoretical analysis of the measurement precision in particle image velocimetry. Experiments in Fluids 2000;29:S003–12. doi: 10.1007/s003480070002.
[21] Rossi S, Ramalli A, Tortoli P. On the depth-dependent accuracy of plane-wave-based vector velocity measurements with linear arrays. IEEE Trans Ultrason Ferroelectr Freq Control 2021;68:2707–15. doi: 10.1109/TUFFC.2021.3076284.
[22] Poree J, Posada D, Hodzic A, Tournoux F, Cloutier G, Garcia D. High-frame-rate echocardiography using coherent compounding with Doppler-based motion-compensation. IEEE Trans Med Imaging 2016;35:1647–57. doi: 10.1109/TMI.2016.2523346.
[23] Krejza J, Arkuszewski M, Kasner SE, Weigele J, Ustymowicz A, Hurst RW, et al. Carotid artery diameter in men and women and the relation to body and neck size. Stroke 2006;37:1103–5. doi: 10.1161/01.STR.0000206440.48756.f7.
[24] Tokunaga K, Koga M, Yoshimura S, Arihiro S, Suzuki R, Nagatsuka K, et al. Optimal peak systolic velocity thresholds for predicting internal carotid artery stenosis greater than or equal to 50%, 60%, 70%, and 80%. J Stroke Cerebrovasc Dis 2016;25:921–6. doi: 10.1016/j.jstrokecerebrovasdis.2015.12.021.
[25] Pellikka PA. Aortic valve area in aortic stenosis in adults. Waltham, MA: UpToDate; 2022.
[26] Foster E. Echocardiographic evaluation of the aortic valve. Waltham, MA: UpToDate; 2022.
[27] Ricci F, Aung N, Gallina S, Zemrak F, Fung K, Bisaccia G, et al. Cardiovascular magnetic resonance reference values of mitral and tricuspid annular dimensions: the UK Biobank cohort. J Cardiovasc Magn Reson 2020;23:5. doi: 10.1186/s12968-020-00688-y.
[28] Baumgartner H, Hung J, Bermejo J, Chambers JB, Evangelista A, Griffin BP, et al. Echocardiographic assessment of valve stenosis: EAE/ASE recommendations for clinical practice. Eur J Echocardiogr 2009;10:1–25. doi: 10.1093/ejechocard/jen303.
[29] Otto CM. The practice of clinical echocardiography. 6th ed. Philadelphia, PA: Elsevier; 2022.